Supporting Information:

Electron Transfer Kinetics on Mono- and Multi-Layer Graphene

Matěj Velický,[a] *Dan F. Bradley,*[b] *Adam J. Cooper,*[a] *Ernie W. Hill,*[c] *Ian A. Kinloch,*[d] *Artem Mishchenko,*[e] *Konstantin S. Novoselov,*[e] *Hollie V. Patten,*[a] *Peter S. Toth,*[a] *Anna T. Valota,*[a] *Stephen D. Worrall,*[a] *and Robert A.W. Dryfe**[a]

[a] School of Chemistry, [c] School of Computer Science, [d] School of Materials, [e] School of Physics and Astronomy, University of Manchester, Oxford Rd, Manchester, M13 9PL, United Kingdom.

[b] Department of Chemistry, University of Liverpool, Crown Street, Liverpool, L69 7ZD, United Kingdom.

* To whom correspondence should be addressed. Tel: +44 (0)161-306-4522; Fax: +44 (0)161-275-4598, e-mail: robert.dryfe@manchester.ac.uk.

Supporting Information Abstract

The additional results and discussion presented in the Supporting Information include micropipette preparation, reference electrode potential determination, Nicholson method, cyclic voltammetry fitting, mediator-free blank voltammetry, AFM of the stable and collapsed micro-droplets, flake preparation procedure, determination of the redox mediator diffusion coefficients, kinetics-droplet size correlation, comparison of the raw and analyzed kinetic data, uncompensated resistance, comparison of electrode kinetics on basal and edge plane of graphite, and X-ray photoelectron spectroscopy (XPS) and Energy-dispersive X-ray spectroscopy (EDX) analysis of atmosphere-aged and freshly cleaved graphite surface.

Micropipette preparation

A P-97 Flaming/Brown micropipette puller (Sutter Instrument, CA, USA) was used to pull a 10 cm long borosilicate fire-polished capillary with a filament (outer diameter 1.5 mm, inner diameter 0.86 mm, Intracel Ltd., UK) to obtain a pair of ca. 5 cm long micropipettes. Figure S1 shows an optical micrograph of the micropipette tip used to deposit the micro-droplet on the flake surface. The tip internal diameter was determined to be 1 µm and external diameter 2 µm.

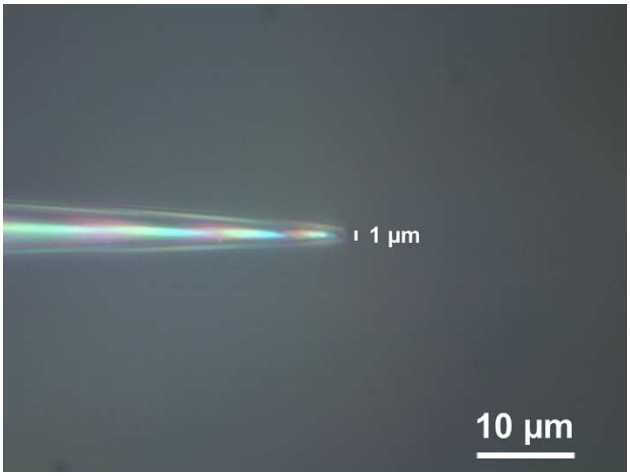

Supporting Figure S1. Optical micrograph of the borosilicate micropipette tip

Reference electrode potential determination

The potential of the Ag/AgCl reference electrode, $E_{\mathrm{AgCl/Ag^0}}$, is determined by the Nernst equation for a reversible chloride-sensitive electrode of the second kind:[1]

$$E_{\mathrm{AgCl/Ag^0}} = E^0_{\mathrm{AgCl/Ag^0}} - \frac{RT}{F}\ln a_{\mathrm{Cl^-}} \qquad \text{(S1)}$$

where $E^0_{\mathrm{AgCl/Ag^0}} = 0.222$ V [2] is the standard redox potential of AgCl reduction to silver metal, R = 8.314 J mol^{-1} K^{-1} is the universal gas constant, T is the thermodynamic temperature, F = 96485 C mol^{-1} is the Faraday constant and $a_{\mathrm{Cl^-}}$ is the activity of the chloride ions. Eq. (S1) can be further expressed as follows:

$$E_{\mathrm{AgCl/Ag^0}} = E^0_{\mathrm{AgCl/Ag^0}} - \frac{RT}{F}\ln \gamma_{\mathrm{Cl^-}} c_{\mathrm{Cl^-}} \qquad \text{(S2)}$$

where $\gamma_{\mathrm{Cl^-}}$ and $c_{\mathrm{Cl^-}}$ are the activity coefficient and concentration of chloride ion respectively. The activity coefficient was determined from the thermodynamic data reported by Taghikhani *et al.*[3] Figure S2 shows a dependence of chloride ion activity coefficient on molality of LiCl aqueous solution. Extrapolation of the dependence on molality of 4.8 mol kg^{-1}, which corresponds to 6 M LiCl, yields an activity coefficient of 0.52. By substituting the thermodynamic data into Eq. (S2), the potential of Ag/AgCl reference electrode in 6 M LiCl aqueous solution at T = 298 K was determined to be 0.193 *vs*. SHE:

$$E_{\mathrm{AgCl/Ag^0}} = 0.222 - \frac{RT}{F}\ln(0.52 \times 6.00)\,\mathrm{V} = 0.193\,\mathrm{V} \qquad \text{(S3)}$$

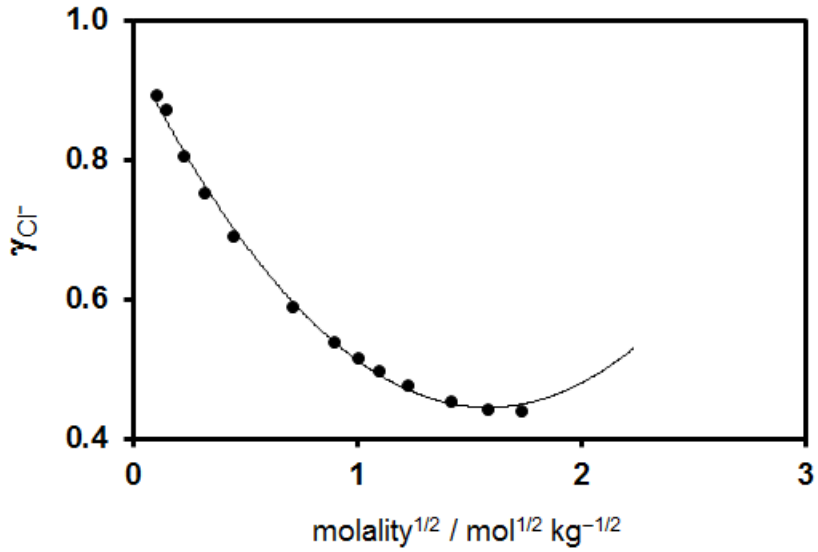

Supporting Figure S2. Dependence of the chloride anion activity coefficients on the square root of LiCl aqueous solution molality as reported in [3]. The activity coefficient at 4.8 mol kg^{-1} (2.2 $mol^{1/2}$ $kg^{-1/2}$), corresponding to 6 M LiCl, was determined by extrapolation of the experimentally determined data.

Nicholson method

The widely used Nicholson method was used to calculate the heterogeneous ET rate from the peak-to-peak separation of the cyclic voltammogram.[4] The empirically determined working function,[5], was used to calculate ψ for a given ΔE_p:

$$\psi = \frac{(-0.6288 + 0.0021\, n\, \Delta E_p)}{(1 - 0.017\, n\, \Delta E_p)} \qquad \text{(S4)}$$

where n is the number of electrons exchanged in the redox reaction. Figure S3 shows the working function (dashed curve) in good agreement with the original kinetic parameters (blue circles) reported by Nicholson.[4] The Nicholson method is only suitable for evaluating quasi-reversible reaction with $\Delta E_p < 220$ mV and an explicit expression for k^0, Eq. (3) in the main text, was used for wider ΔE_p.

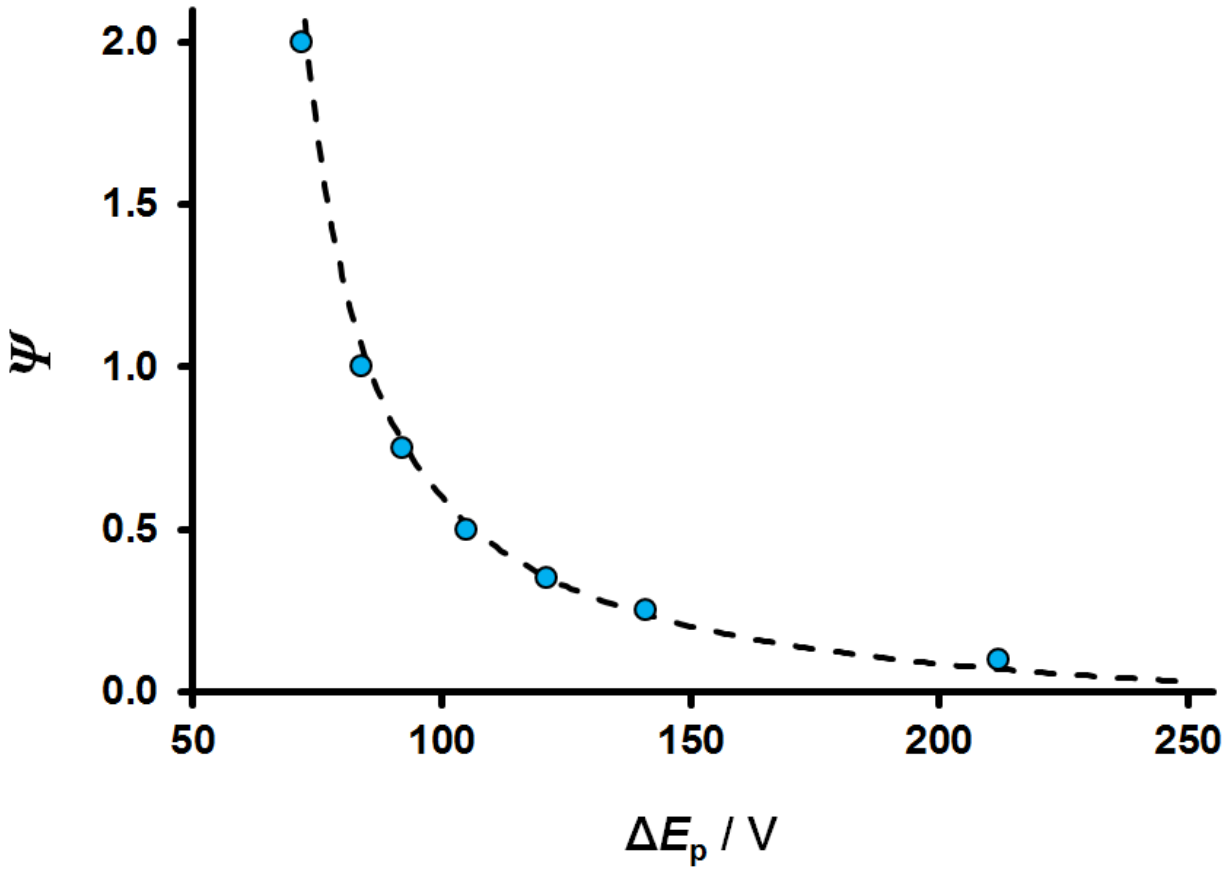

Supporting Figure S3. Nicholson method working function (dashed curve) calculated from Eq. (S4) as a tool determine the kinetic parameter ψ from ΔE_p (< 220 mV). Blue circles are the kinetic parameters as reported by Nicholson.[4]

Cyclic voltammetry fitting

In order to verify that the analytical method of Klingler-Kochi used to determine k^0 from large ΔE_p (> 220 mV) is appropriate for this system, a sample of the voltammograms was simulated in one dimension from first principles (Fick's Laws, Butler-Volmer kinetics), as a thin-layer system, using a commercial finite element modelling (FEM) package (DidiElch Professional, ElchSoft, most recent release Q2 2014). Best fit was achieved for each experiment across a range of scan rates, keeping all parameters consistent. An example of parameter values used is shown in Table S1. Comparison of the experimental (solid curves) and simulated (dashed curves) voltammograms for $Ru(NH_3)_6^{3+/2+}$ reduction/oxidation is shown in Figure S4. The experimental and simulated data are in good agreement and the k^0 value determined from the fitting is reasonably close to the analytically determined value. The small discrepancies between the experimental and simulated voltammograms and ET rate values (k^0_{exp} and k^0_{sim}, respectively) most likely occur due to uncertainties in diffusion coefficient, droplet area and also possible deviation of the diffusion regime within the droplet from the ideal thin-layer cell behavior, which is evident for the slowest of scan rates. Importantly, the relative comparison of the kinetics, which is crucial in this work, will not be affected by inaccuracies in the absolute value of calculated k^0.

Supporting Table S1 Full parameter values used to generate simulated voltammograms shown in Figure S4.

Parameter	Value
ν	0.2, 0.4 and 1 V s^{-1}
E_0	–0.2 V
α	0.46
k^0_{sim}	3.1×10^{-5} cm s^{-1}
D_O, D_R	2.4×10^{-6} cm^2 s^{-1}
A	670 μm^2
d	18 µm
R	100 kΩ
C_{dl}	50 pF

Where d is the apex thickness of the micro-droplet, R and C_{dl} is the resistance and double-layer capacitance of the electrochemical cell and the remaining symbols have previously defined meanings.

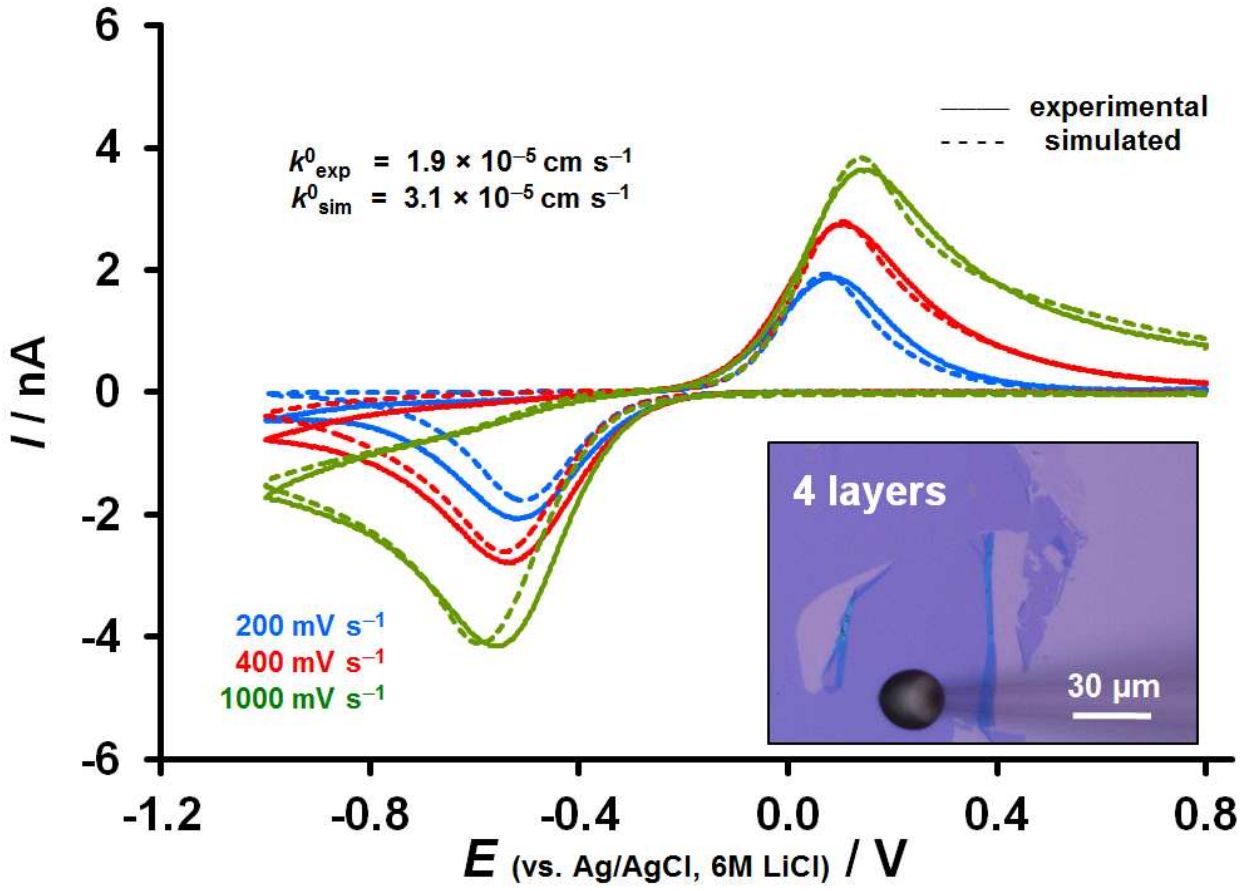

Supporting Figure S4. Experimental (solid curves) and simulated (dashed curves) voltammograms of $Ru(NH_3)_6^{3+/2+}$ reduction/oxidation on 4-layer graphene at scan rates of 200 mV s^{-1} (blue), 400 mV s^{-1} (red) and 1000 mV s^{-1} (green). The fitting parameters included k^0, α = 0.46, D and droplet/flake interfacial area (allowed up to 5% variation in droplet radius). The experimental voltammograms are those already shown in Figure 2b of the main text and the inset shows the optical micrograph of the analyzed droplet.

Mediator-free blank voltammetry

Blank voltammograms, *i.e.* measurement with a droplet containing only 6 M LiCl were recorded and compared with the voltammogram obtained for $Ru(NH_3)_6^{3+/2+}$ (Figure S5). Because the low redox potential of this mediator (lower than the other two used in this work) and the fact that the aqueous solutions used in measurements were not de-aerated, there is a possibility that oxygen reduction reaction (ORR) could interfere with reduction of $Ru(NH_3)_6^{3+/2+}$ and affect the measurement/analysis. The comparison of the blank and $Ru(NH_3)_6^{3+/2+}$ cyclic voltammogram in Figure S5 suggests that there is an onset potential region of –0.6 to –0.7 V where parasitic current, most likely from ORR, occurs. The onset potential and current value did not seem to vary significantly with the flake thickness. The absolute current value is negligible in comparison to the $Ru(NH_3)_6^{3+/2+}$ reduction peak occurring above –0.6 V for even the least reversible cases (at 300 mV s^{-1}). Also, the reduction/oxidation peaks were symmetrical and peak currents were of very similar values, proving that no competing processes occur. We can therefore conclude that there is very little interference between the analytical signal and ORR.

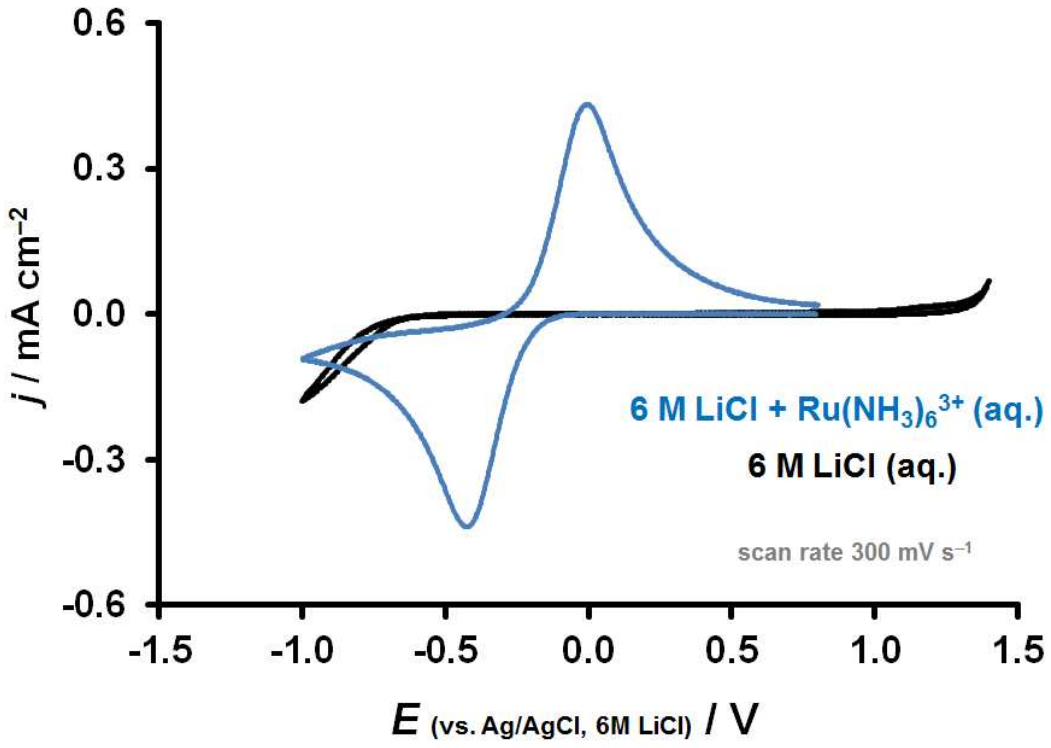

Supporting Figure S5. Comparison of (a) mediator-free and (b) $Ru(NH_3)_6^{3+/2+}$ reduction/oxidation voltammograms both obtained at 300 mV s^{-1} on bilayer graphene.

AFM of the stable and collapsed micro-droplets

Atomic force microscopy (AFM), which was previously applied to measurement of the size and shape of droplets on solid substrates,[6, 7] was used to estimate the height of the micro-droplets deposited on the monolayer graphene. Figure S6 shows AFM height profile images of a stable droplet of diameter about 10 μm (a) and a droplet of a similar diameter, which induced damage to the graphene monolayer (b). The stable droplet has an estimated height of *ca*. 5 μm, which is about 50% of its diameter, corresponding to a drop/graphene contact angle of *ca*. 90° (measurement of the whole droplet is limited by its height and is therefore increasingly difficult for larger drops).[8] The height is expected to be lower for larger droplets. For the damage-induced case, the droplet shows a collapse of its shape due to the adhesion forces with the ruptured graphene so that the height decreases to less than 1 μm.

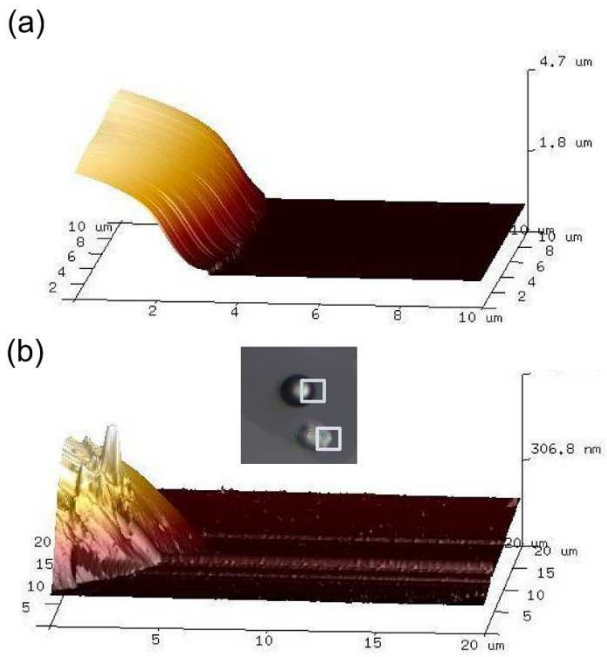

Supporting Figure S6. AFM measurement ("PeakForce" tapping mode) of droplets of *ca*. 10 µm in diameter deposited on a monolayer graphene flake. (a) Stable droplet, (b) collapsed droplet due damage induced to underlying graphene. The inset image shows a micrograph of both droplets with highlighted areas of the AFM scan.

Flake preparation procedure

Prior to the exfoliation, thermally oxidized silicon wafers (2.5 cm × 2.1 cm, 290 nm layer of SiO_2, IBD Technologies, Ltd, UK) were de-greased by sonication in acetone and isopropyl alcohol (IPA), 10 min in each solvent, using an Elma transsonic bath model TI-H-5 (Elma Hans Schmidbauer GmbH, Germany), dried using compressed nitrogen gas and etch-cleaned using MiniLab 125 Ar/O_2 plasma etcher for 10 min (Moorfield, UK).

Natural graphite crystals used for exfoliation (NGS, Naturgraphit, GmbH, Germany) were cleaved several times (3 to 5 times depending on the graphite quality) using high-tack, low-stain cello-tape to obtain fresh, flat and pristine graphite surface. The graphite was then pressed onto a clean tape surface until a uniform area of about 10 cm^2 of thin graphite (< 100 μm) layer was obtained, which was then pressed onto the Si/SiO_2 wafers. The tape was dissolved in methyl isobutyl ketone (MIBK), and wafers washed in fresh MIBK (5 min), IPA (5 min) at the same temperature, then blow-dried with nitrogen and baked on a hotplate at 120-130 for 10 min. Finally, a peel using the above tape was carried out to expose the fresh flake surface. Upon examination under an optical microscope, wafers with suitable flakes were immobilized on a glass microscope slide and electrical contact made.

Determination of the redox mediator diffusion coefficients

The diffusion coefficients of the three redox mediators, $Fe(CN)_6^{3-/4-}$, $Ru(NH_3)_6^{3+/2+}$ and $IrCl_6^{2-/3-}$ in 6 M LiCl aqueous solution were determined by three different electrochemical methods. Firstly, cyclic voltammetry was performed at a macroscopic platinum disc electrode (2.2 mm in diameter, CH Instruments Inc., TX, USA), which was polished prior to measurement using a 1/4 μm and 1/10 μm liquid diamond suspension and synthetic nap-type cloth (Kemet International Ltd, UK). Pt-disc electrode voltammetry exhibited a (near) reversible electron transfer of all three mediators up to scan rates of 500 mV s^{-1}, indicated by the reduction/oxidation ΔE_p of 59 – 70 mV, and is demonstrated with the $Fe(CN)_6^{3-/4-}$ reduction/oxidation CV in Figure S7a. Both reduction and oxidation peak currents were plotted against the square root of scan rate as shown in Figure S7b and the Randles-Ševčík equation, Eq. (4) in the main text, used to determine the diffusion coefficient from this dependence. Chronoamperometry was also performed at a Pt-disc electrode and the current-time transients, corresponding to reductive and oxidative potential steps are shown in Figure S7c (for $Ru(NH_3)_6^{3+/2+}$). The current-time dependence is described by the Cottrell equation:[9]

$$I = \frac{nFAc\sqrt{D}}{\sqrt{\pi t}} \qquad \text{(S5)}$$

where I is the current, n is the number of electrons involved in reduction/oxidation of the mediator, F is the Faraday constant, A is the Pt-disc electrode area, c is the bulk concentration of the mediator, D is the diffusion coefficient of oxidized/reduced form of the mediator and t is the time. As shown in Figure S7d, the slope of the current dependence on $(\pi t)^{-1/2}$ allows the diffusion coefficient to be calculated.

Despite the quasi-reversibility discussion in the main text, the voltammetric peak current was found to be linearly proportional to $\nu^{1/2}$ for most droplets but the diffusion within the small droplets showed deviation from the expected behavior as discussed in the main text.

The above analysis was performed for all three redox mediators and the results are listed in Table S2, along with the diffusion coefficients determined from the micro-droplet CV.

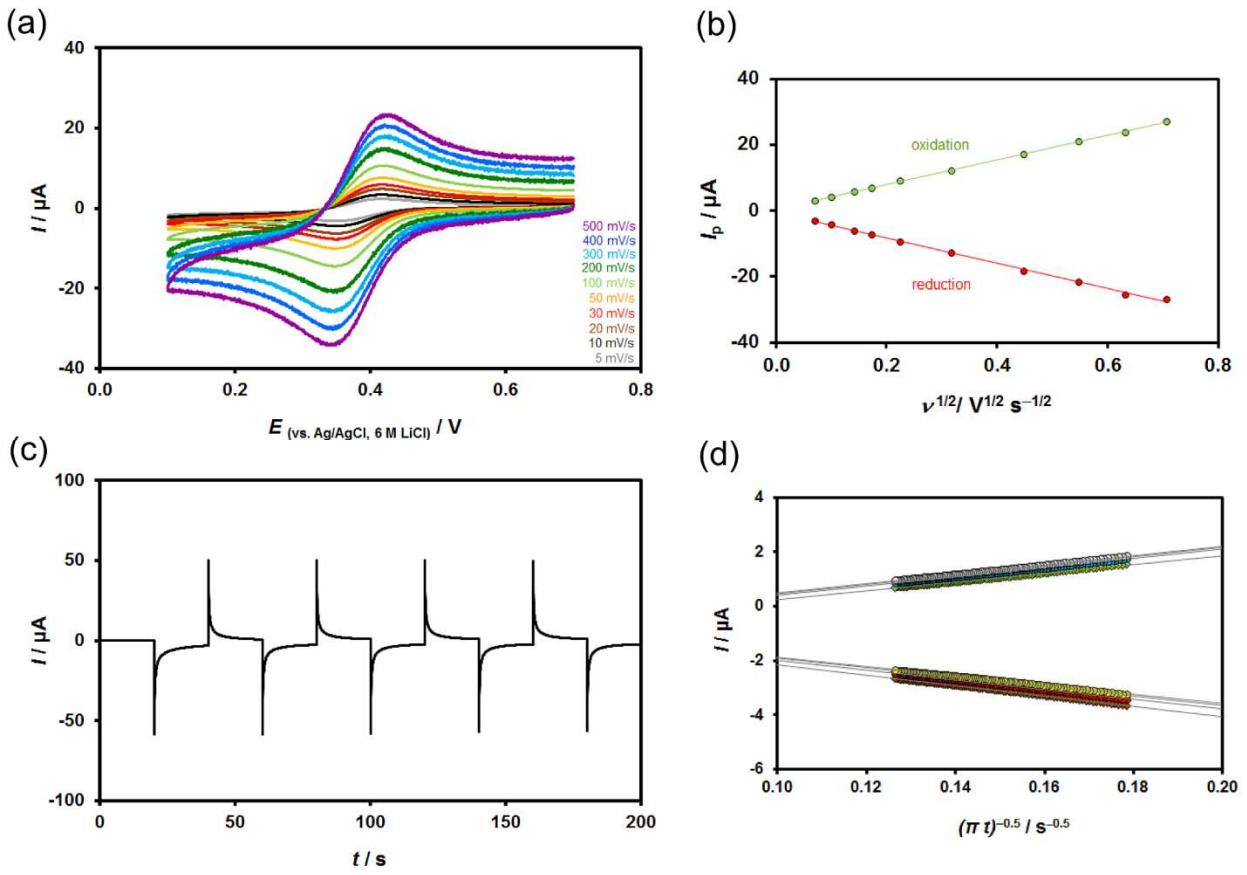

Supporting Figure S7. Electrochemical methods used to determine the respective diffusion coefficients of the redox mediators in 6 M LiCl at a Pt-disc macroelectrode (2.2 mm in diameter). (a) Cyclic voltammogram of $Fe(CN)_6^{3-/4-}$ reduction/oxidation at scan rate range of 5 – 500 mV s^{-1}. (b) Randles-Ševčík plots (peak current *vs*. square root of scan rate dependence) for the same voltammogram. (c) Chronoamperometric measurement of $Ru(NH_3)_6^{3+/2+}$ reduction/oxidation *via* alternating the potential between + 0.4 and –0.6 V with period of 20 s. (d) Cottrell plot of the same CA measurement. The potential was referenced against Ag/AgCl wire (electrode potential in 6 M LiCl is +193 mV *vs*. SHE).

Supporting Table S2 Comparison of diffusion coefficients determined using various electrochemical methods.

redox mediator	method	D_R / 10^{-6} cm^2 s^{-1}	D_O / 10^{-6} cm^2 s^{-1}
$Fe(CN)_6^{4-/3-}$	macro CV [a]	1.49 ± 0.00	1.56 ± 0.00
	macro CA [b]	2.31 ± 0.04	1.99 ± 0.05
	macro mean [c]	**1.84 ± 0.19**	
	micro-droplet CV [d]	2.07 ± 0.14	2.65 ± 0.08
$Ru(NH_3)_6^{2+/3+}$	macro CV [a]	2.07 ± 0.00	2.38 ± 0.00
	macro CA [b]	2.63 ± 0.20	2.35 ± 0.09
	macro mean [c]	**2.36 ± 0.11**	
	micro-droplet CV [d]	2.07 ± 0.14	2.65 ± 0.08
$IrCl_6^{3-/2-}$	macro CV [a]	2.06 ± 0.00	2.19 ± 0.00
	macro CA [b]	2.69 ± 0.17	2.14 ± 0.04
	macro mean [c]	**2.27 ± 0.14**	
	micro-droplet CV [d]	3.86 ± 0.37	3.41 ± 0.31

The values are either arithmetic means of values from multiple measurements, or obtained as best fits. The errors are either standard deviations or absolute errors determined from the best fit errors.

[a] values determined from cyclic voltammogram and Eq. (4) at a Pt-disc macro-electrode.

[b] values determined from chronoamperometry and Eq. (S5) at a Pt-disc macro-electrode.

[c] an average of the macro CV and CA value used in ET kinetics calculations.

[d] values determined from cyclic voltammogram and Eq. (4) at micro-droplets deposited on graphene flakes.

Correlation between measured electrode kinetics and droplet/flake interfacial area

In order to eliminate any undesirable kinetic effects, which could arise from varied droplet size, a random set of droplet/graphene interfacial areas (300 – 3000 μm^2) were used for analysis on a given flake. The ET rate measured for all the droplets was then plotted as a function of the droplet/flake interfacial area to uncover any hidden correlations. No correlations were found for the two 'slow kinetics' mediators, $Fe(CN)_6^{3-}$ and $Ru(NH_3)_6^{3+}$, as shown in Figures S8a and S8b, respectively. This was, however, not the case for $IrCl_6^{2-/3-}$. It is clear from Figure S8c that the droplet size loosely correlates with the kinetics below interfacial areas of *ca.* 1000 μm^2, which could inevitably alter the overall layer-dependence picture of kinetics, despite the random distribution of droplet sizes throughout the measurement. The correlation is attributed to the near-reversible kinetics of $IrCl_6^{2-/3-}$ reduction/oxidation, manifesting in higher currents (than for $Fe(CN)_6^{3-}$ and $Ru(NH_3)_6^{3+}$) flowing through the graphene electrode, which are comparable with the bulk availability of the mediator within the droplet. This, in turn, could either steer the diffusion regime within a droplet away from the ideal thin-layer cell behavior or alternatively increase the cell ohmic drop, both of these scenarios could consequently alter the measured kinetics.

For the above reasons, the measured ET rate of $IrCl_6^{2-/3-}$ reduction/oxidation was corrected under the assumption that the fitted power function (Figure S8c) describes the dependence of k^0 on the droplet area and the deviation from the function reflects the true (i.e. free of area-induced effects) kinetics. The 'true' ET rate, k^0(A) for a droplet with an interfacial area A, is calculated as follows:

$$k^0 = k_m^0(A) - \left[f(A) - f(A^0) \right] \qquad \text{(S6)}$$

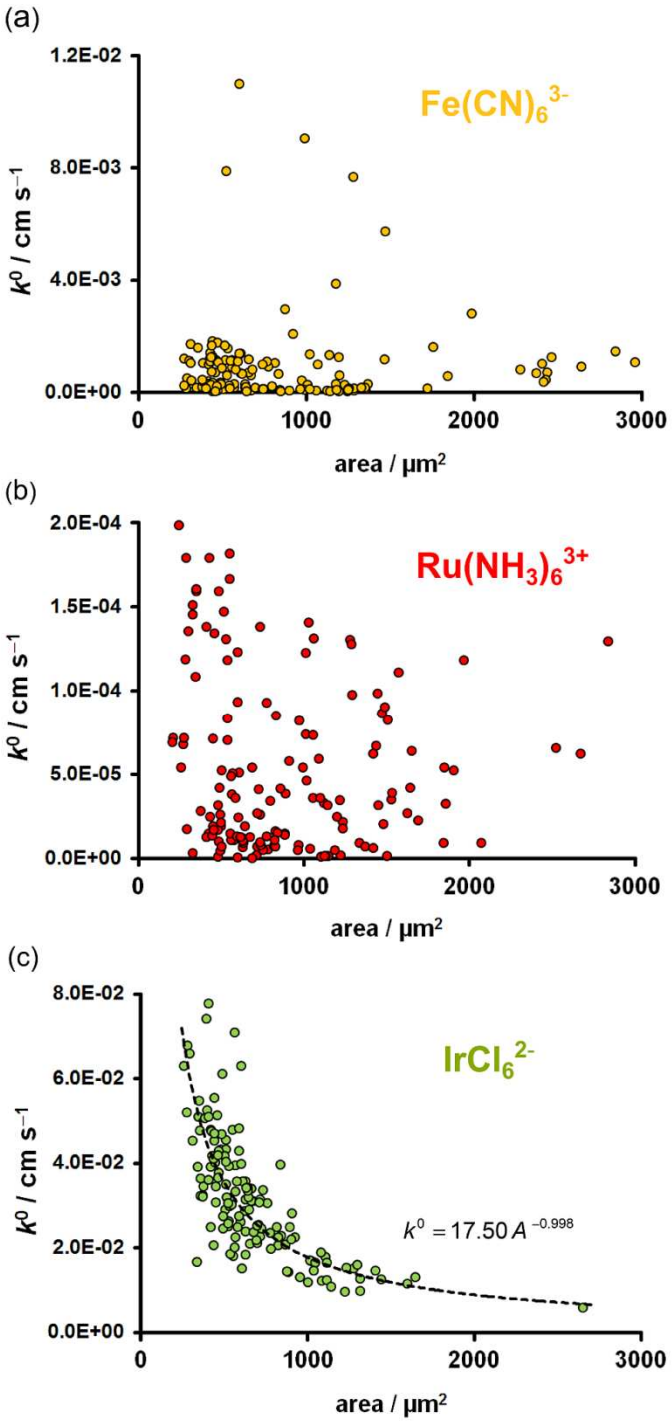

Supporting Figure S8. Correlation between the measured ET rate and the droplet/electrode interfacial area for (a) $Fe(CN)_6^{3-}$, (b) $Ru(NH_3)_6^{3+}$ and $IrCl_6^{2-}$, plotted for all 435 analyzed droplets.

where $k_m^0(A)$ is the measured ET rate for a droplet of an interfacial area A, $f(A)$ is the power function (from Figure S8c) for an area A, and A^0 is an arbitrary interfacial area within a region most populated with droplets (chosen as A^0 = 600 μm^2). Note that the term $f(A) - f(A^0)$ is essentially the size-induced part of the measured kinetics, $k_m^0(A)$.

The comparison of the measured and corrected layer dependence of the kinetics is shown in Figure S9 and as one can see the standard deviations of the arithmetic means have reduced significantly. The correction of k^0 for droplet size induced effects is, of course, approximate and the measured kinetics on the order of 10^{-2} cm s^{-1} are at the very limit of detection for cyclic voltammetry, reflecting the inherent near-reversibility of $IrCl_6^{2-/3-}$ reduction/oxidation on graphitic surfaces.

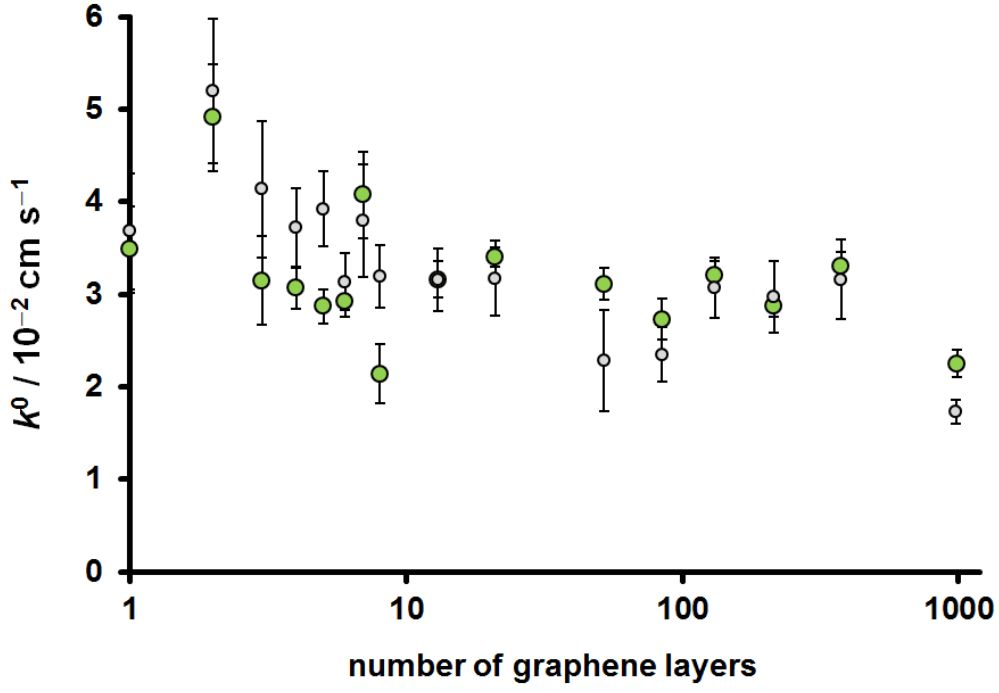

Supporting Figure S9. Comparison of the measured (gray) and corrected (green) kinetics-layer dependence for $IrCl_6^{2-/3-}$ reduction/oxidation.

Comparison of the raw and analyzed kinetic data

The voltammetric data analyzed using Nicholson and Klingler-Kochi methods were compared with the raw experimental data. Figure S10 shows a comparison between k^0 and ΔE_p dependences on the number of graphene layers. Although plotting the peak-to-peak separations is less meaningful than using either Nicholson analysis or average k^0 from Klingler-Kochi analysis, it is useful to provide the raw experimental data. Indeed, ΔE_p follows roughly the same trend as the analysed (k^0) data. Some deviation is observed for the $IrCl_6^{2-}$ case, most likely due to the area-correction of the kinetics as described in the previous section and generally higher inaccuracy in determination of such fast k^0.

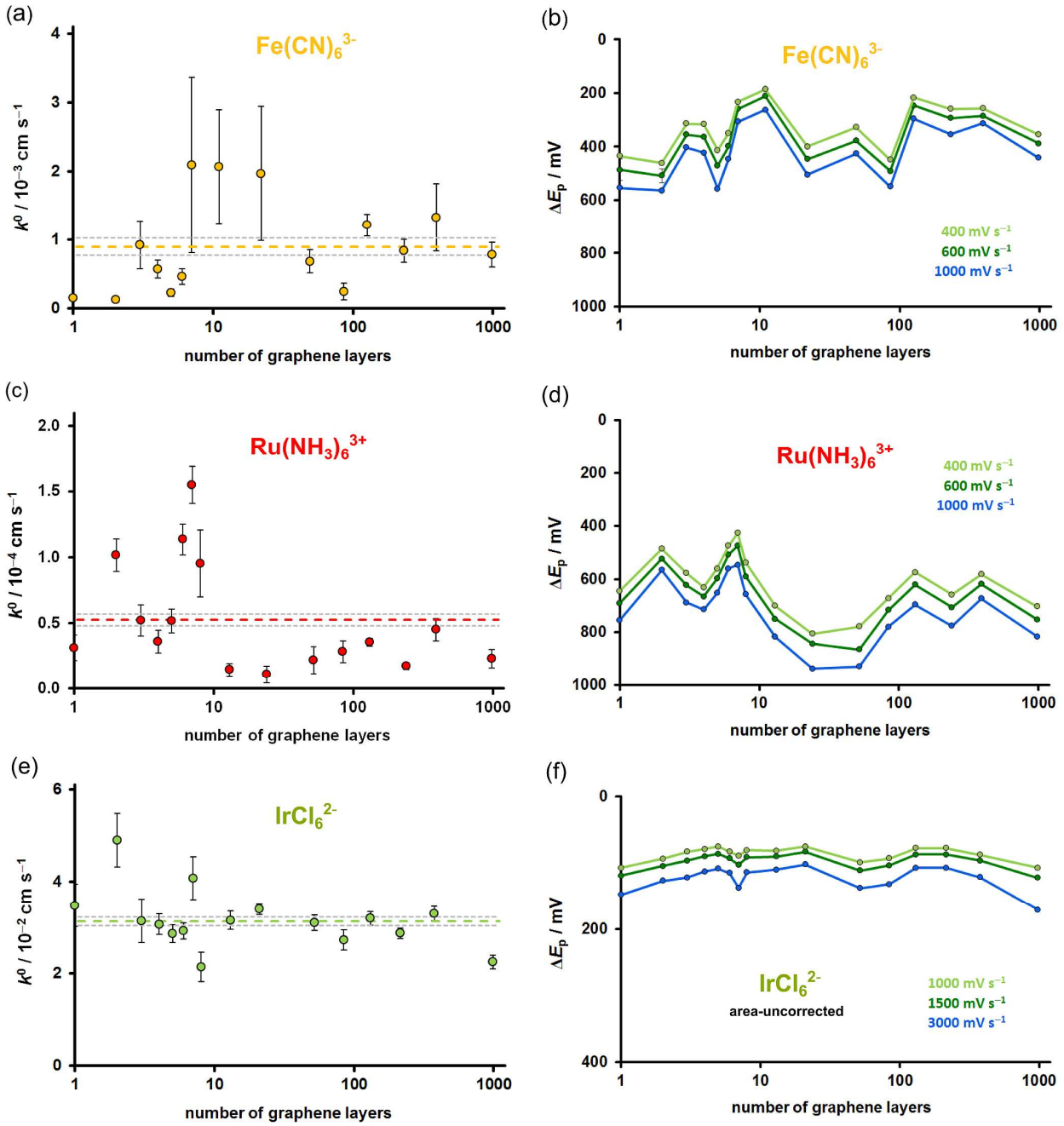

Supporting Figure S10. Comparison of the analyzed (a,c and e) and raw voltammetric data (b, d and f) as a function of the number of graphene layers. The data on the right are k^0 values as presented in Figure 3 (main text) and data on the left corresponding averaged ΔE_p for all three redox mediators.

Uncompensated resistance

The uncompensated resistance, R_u, in the electrochemical micro-droplet cell consists of the following components: wiring connecting the potentiostat with (A) droplet solution and (B) the silver epoxy, (C) solution itself, (D) silver epoxy, (E) ohmic contact between the silver epoxy and the flake and (F) the flake itself. The first four elements (A-D) can be neglected as their combined resistance is typically 1 – 10 Ω. The resistance of the ohmic contact (E) depends on the contact perimeter between the flake and silver epoxy and would typically be around 1 – 100 kΩ for a few micrometer contacts and much smaller for larger contacts. We have measured a 2-point resistance of series of samples prepared according to the schematic in Figure S11. A few examples of current-voltage curves obtained for this wire/silver/flake/silver/wire configuration are shown in Figure S12. The corresponding resistances are calculated from the linear dependence using Ohm's law. The lowest recorded 'through resistance' of such devices was as low as 4 Ω, for a thick graphite (> 1000 layers) and ohmic contact of a few hundred micrometers. The highest recorded resistance was 133 kΩ (~40 layers thick flake), meaning the highest measured resistance per contact/flake was *ca.* 70 kΩ.

In our configuration, the typical currents are in the region of 0.1 – 10 nA. The highest measured contact resistance (~ 70 kΩ per contact), would result in a shift in potential between 10^{-6} – 10^{-4} V, too low to affect the measurement. Furthermore, the effect of R_u on voltammetry is most prominent when the electrode reaction approached reversibility, *i.e.* when k^0 is large.[10] This is demonstrated *via* simulated cyclic voltammograms in Figure S13 and change of the shape of the voltammetric curves changes with increasing R_u. Although it is generally quite difficult to distinguish whether the increase in peak separation arises from large R_u or slow ET kinetics, one

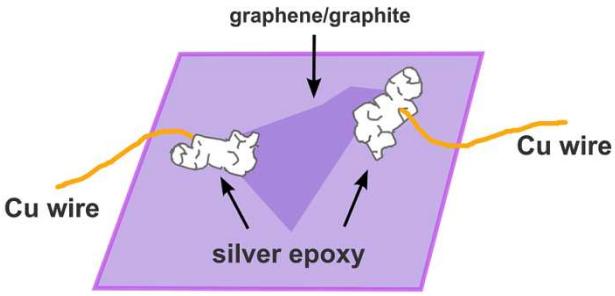

Supporting Figure S11. A schematic of a 2-point device designed to estimate the resistance of an ohmic contact between the graphene/graphite flake and silver epoxy.

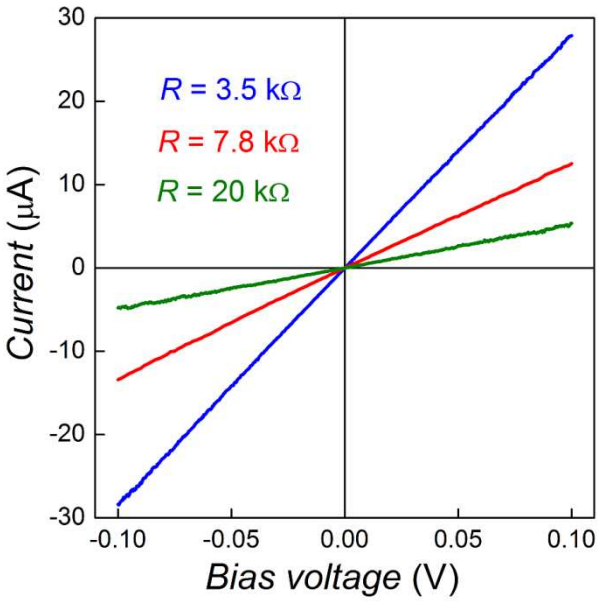

Supporting Figure S12. Current-voltage dependence and the corresponding resistances of the 2-point device. The data were obtained on flake of ~100-layer (blue), 3-layer (red) and ~50-layer (green) thicknesses.

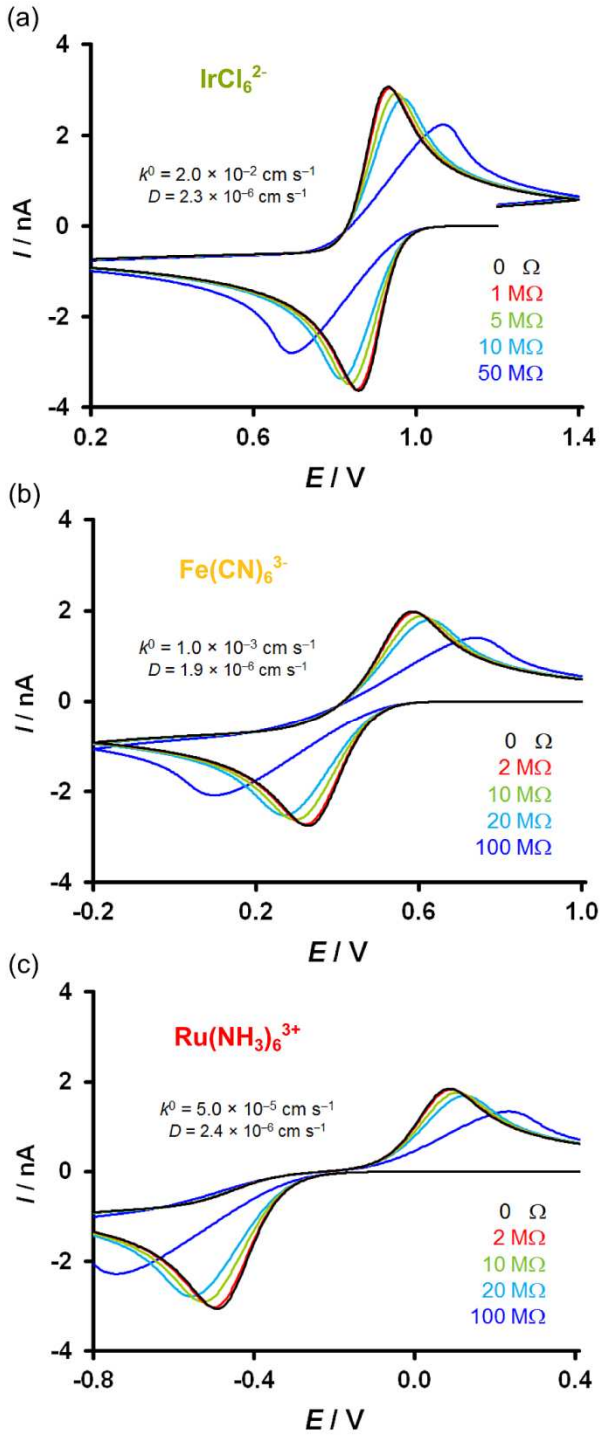

Supporting Figure S13. Simulated cyclic voltammograms of reduction/oxidation of the three redox mediators considering large uncompensated resistances. The simulation was carried out using EC-Lab software, version 10.34 (Bio-Logic SAS, France).

can see that CV shape becomes notably distorted and the peaks are no longer vertically symmetrical. The increase in peak-to-peak separation was smaller than 5 mV up to 1 MΩ or 2 MΩ for $IrCl_6^{2-}$ or $Fe(CN)_6^{3-}$/$Ru(NH_3)_6^{3+}$, respectively.

Finally, the flake resistance will depend on its thickness and obviously will be largest for graphene monolayer. A typical monolayer sheet resistance would be between 1 – 10 kΩ/□ for undoped graphene.[11] In order to test the R_u arising from the flake resistance only, three similar-sized droplets were placed at different distances from the silver epoxy contact on a monolayer graphene flake (Figure S14). No significant change in kinetics, and therefore peak separation, was observed (Table S3).

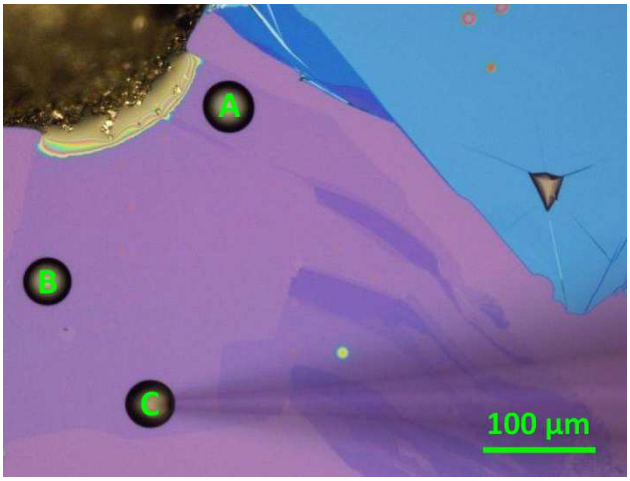

Supporting Figure S14. An optical micrograph of three microdroplets of a similar size, deposited at different distances from the ohmic flake/silver epoxy contact.

Supporting Table S3 Comparison of the $IrCl_6^{2-/3-}$ reduction/oxidation kinetics obtained from droplets deposited at different distances from the silver epoxy contact (epoxy edge to center of the droplet).

droplet	distance to silver epoxy / µm	k^0 / 10^{-2} cm s^{-1}	Δ / 10^{-2} cm s^{-1}
A	57	2.577	0.001
B	119	2.353	0.004
C	225	2.464	0.002

Comparison between basal and edge plane electron-transfer activity of graphite

Electrode kinetics of the pristine basal plane with that of the edge plane graphite (~60 layers) is compared. Figure S15 shows the series of CVs recorded on pristine basal plane (a) and both basal and edge plane exposed. The heterogeneous ET rate for the $Fe(CN)_6^{3-/4-}$ mediator was determined as $(0.75 \pm 0.03) \times 10^{-3}$ cm s^{-1} for the pristine basal plane and $(0.57 \pm 0.02) \times 10^{-3}$ cm s^{-1} for surface containing both basal and edge plane. Despite the traditional view on the relative electroactivity of graphite surfaces,[12, 13] the edge plane did not show faster kinetics than basal plane.

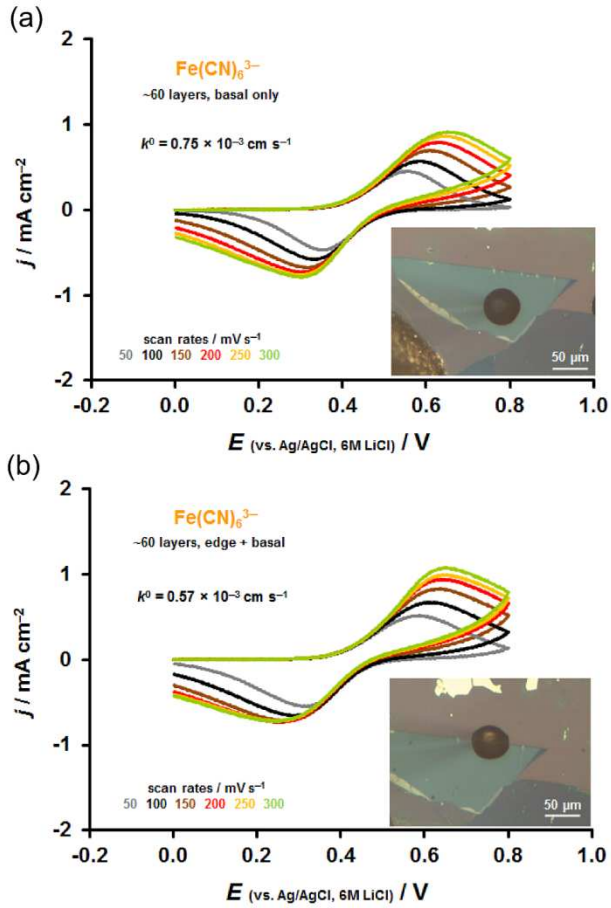

Supporting Figure S15. A comparison of the ET rate on the basal plane and edge plane of graphite (*ca*. 30 graphene layers) using reduction/oxidation of $Fe(CN)_6^{3-/4-}$ mediator in 6 M LiCl. (a) micro-droplet on the pristine basal plane of the flake, (b) micro-droplet deposited over the flake/SiO_2 boundary, and therefore exposed to the edge plane. The insets in the bottom right are micrographs of the deposited droplets. The color scheme and measurement parameters are the same as for the CVs in the main text.

XPS and EDX characterization of aged and freshly cleaved graphite surface

Although the pristine, defect-free, graphite basal plane lattice exhibits pure sp^2 hybridization, the existence of defects, edges, function groups and adsorbents, will alter the sp^2/sp^3 hybridization ratio. This is confirmed by detailed analysis of the C 1s peak and C Auger (KLL) peak (binding energies 284 and 1224 eV, respectively). The C 1s peak was fitted with appropriate components and contributions of sp^2 and sp^3 hybridization content calculated, C KLL peak was differentiated and D-parameter, whose value increases with sp^2/sp^3 ratio, was determined.[14-16] The analyses of both peaks are shown in Figures S16 and S17. Table S4 shows the comparison of the sp^2 content with the overall carbon concentration at each site. The data, also plotted in Figure 5 of the main text, indicate that fraction of the sp^2 hybridized carbon increases with the increasing carbon concentration (both from C 1s and C KLL analysis). This suggests that the most of the major impurities, i.e. N, O and F are constituents of either functional groups or adsorbed molecules, increasing the overall number of non-sp^2 hybridized carbon atoms at the surface.

The XPS analysis was supported by complimentary EDX measurement (Figures S18, S19 and Table S5), carried out using FEI Quanta 200 Scanning Electron Microscope over a large surface area (ca. 4 mm^2) of both the aged and cleaved graphite samples. Unlike XPS, which contains information about the surface of the sample (a few nanometers penetration depth), EDX has a larger bulk component to the compositional information (a few micrometers penetration depth). Indeed, the average carbon content determined from EDX is ca. 3.5 at% higher (and lower for the impurity atoms) than that of XPS, confirming that contamination of both surfaces with foreign atoms is predominantly surface-bound.

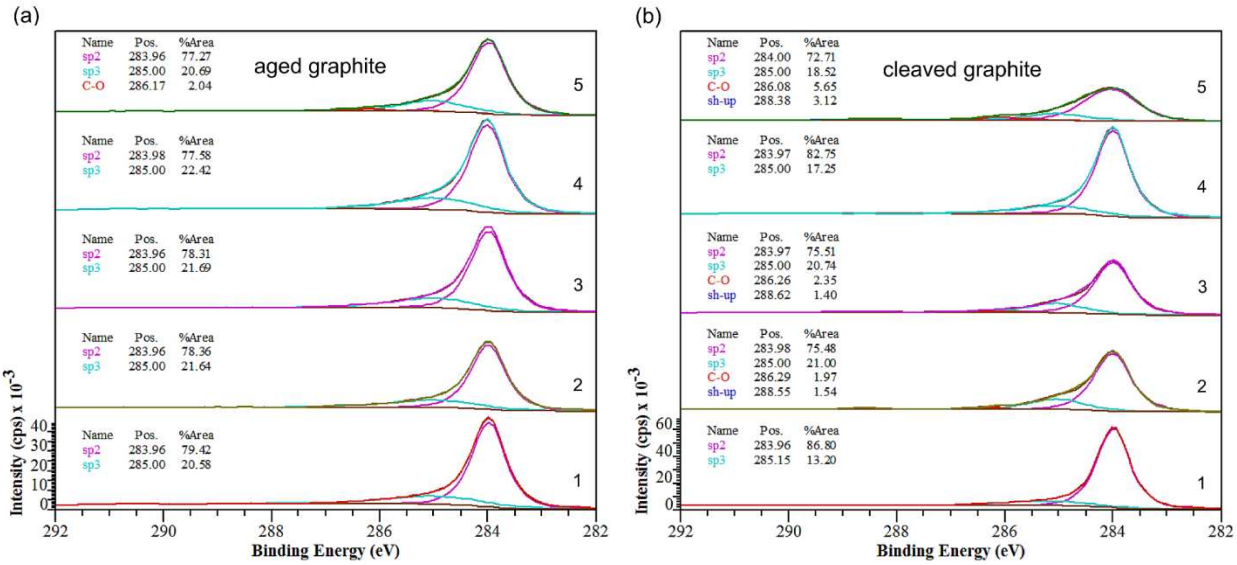

Supporting Figure S16. Analysis of the carbon 1s peak in the XPS spectra obtained at individual surface sites (1 – 5) on (a) aged and (b) cleaved graphite sample.

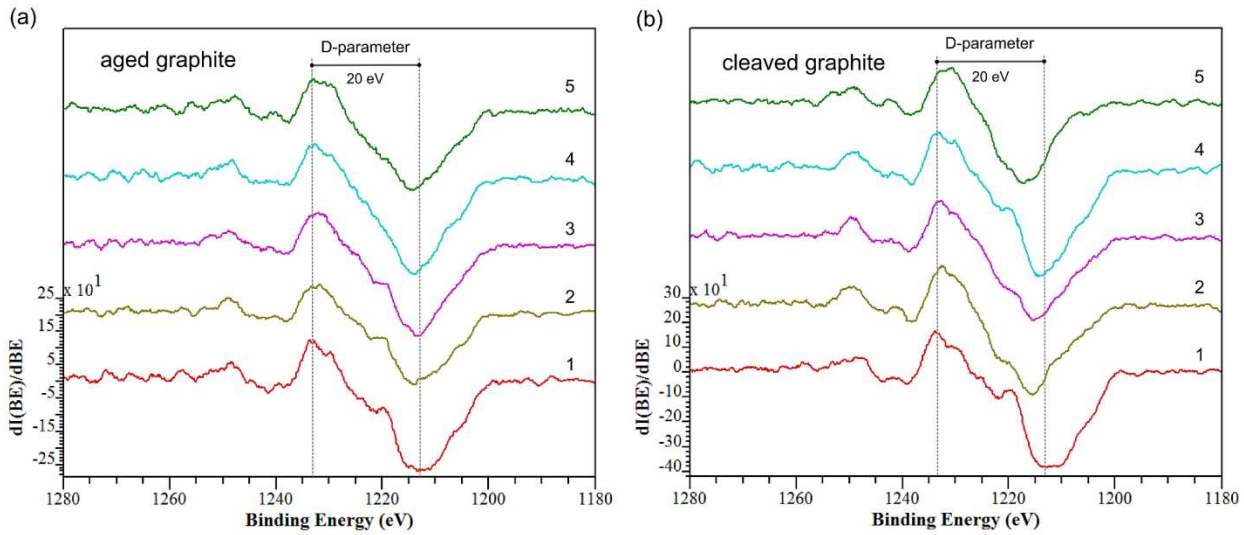

Supporting Figure S17. Analysis of the carbon Auger peak (KLL) in the XPS spectra obtained at individual surface sites (1 – 5) on (a) aged and (b) cleaved graphite sample. The graphs show the derivative of the intensity (in respect to the binding energy) against the binding energy. The D-parameter values are determined and listed in Table S4.

Supporting Table S4 Comparison of the extent of sp^2 hybridization of carbon atoms determined from C 1s peak quantification and D-parameter (C Auger peak) of the XPS spectra obtained at 5 different surface sites on aged and cleaved graphite samples.

surface site	aged graphite		
	total C / At%	**sp^2 (C 1s) / %**	**D-parameter (C KLL) / eV**
1	92.1	79.4	19.9
2	94.1	78.4	18.6
3	90.7	78.3	18.6
4	92.2	77.6	19.0
5	91.5	77.3	18.3
cleaved graphite			
1	97.4	86.8	21.3
2	89.0	75.5	17.1
3	90.9	75.5	17.9
4	94.7	82.8	19.3
5	85.8	72.7	15.1

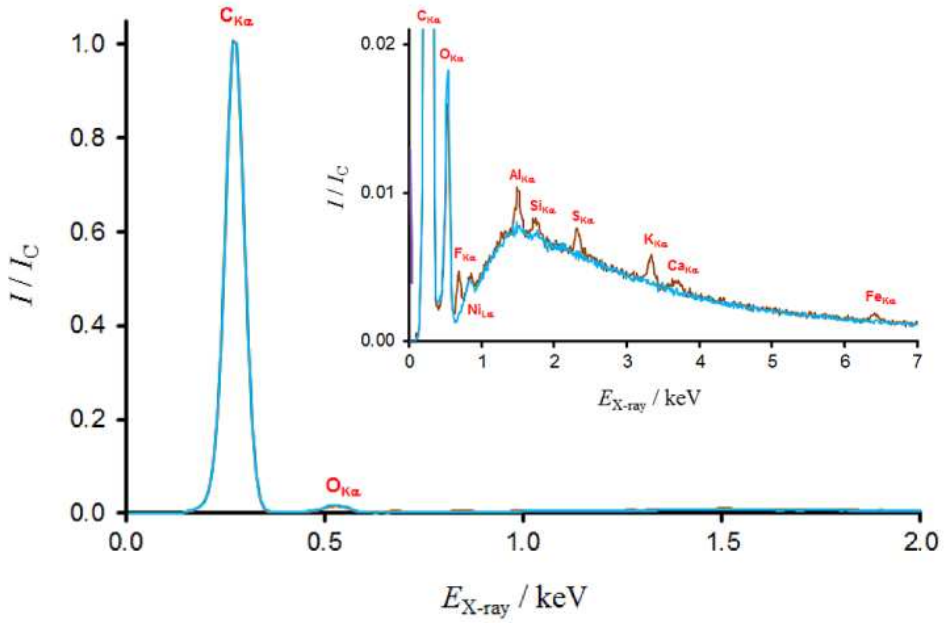

Supporting Figure S18. EDX spectra recorded on both aged (brown curve) and cleaved (blue curve) graphite sample. The spectra in main graph show the two main constituents, carbon and oxygen, the smaller inset spectra showing the impurity elements in detail. The electron beam was accelerated to 20 keV.

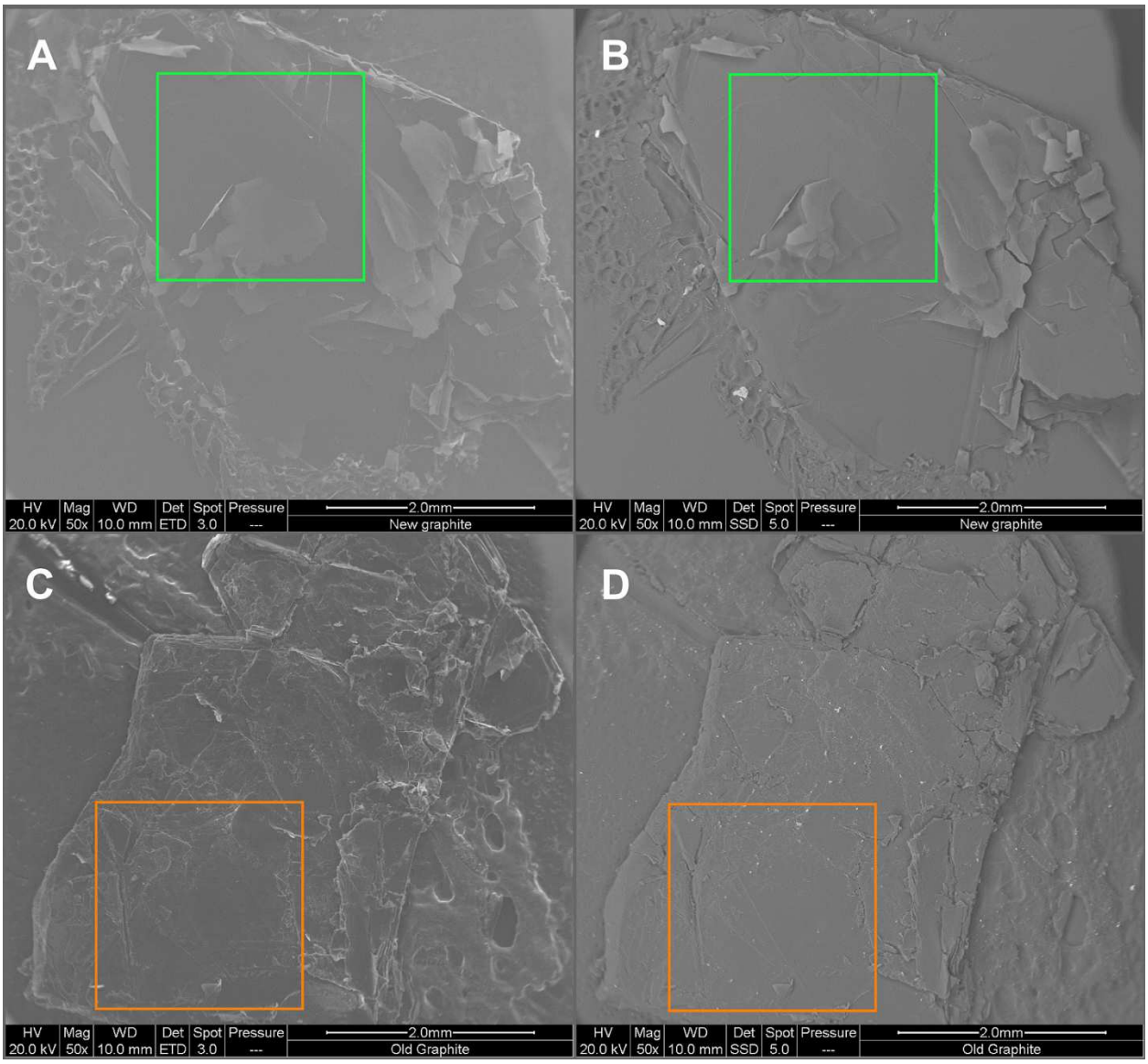

Supporting Figure S19. Electron micrographs of the graphite sample areas analyzed with EDX. (a) and (b) are the secondary and backscattered electron micrographs of the cleaved graphite, respectively, (c) and (d) are the secondary and backscattered electron micrographs of the aged graphite, respectively.

Supporting Table S5 Quantification analysis of the EDX spectra averaged over a large surface area (4 mm^2) on aged and cleaved graphite samples.

element	aged	cleaved
	At %	At %
C	96.86	96.49
N	0.00	0.00
O	2.76	3.44
F	0.17	0.00
Na	0.00	0.00
Al	0.06	0.02
Si	0.02	0.01
S	0.03	0.00
K	0.04	0.00
Ca	0.02	0.00
Fe	0.02	0.00
Ni	0.02	0.04

References

1. Ives, D. J. G.; Janz, G. J., Academic Press: New York, 1961.
2. Crc Handbook of Chemistry and Physics. In *CRC Handbook of Chemistry and Physics* [Online] 94th ed.; Haynes, W. M., Ed. CRC Press: 2013; p. 2668.
3. Taghikhani, V.; Modarress, H.; Vera, J. H. Individual Anionic Activity Coefficients in Aqueous Electrolyte Solutions of Licl and Libr. *Fluid Phase Equilib.* 1999, 166, 67-77.
4. Nicholson, R. S. Theory and Application of Cyclic Voltammetry for Measurement of Electrode Reaction Kinetics. *Anal. Chem.* 1965, 37, 1351-1355.
5. Lavagnini, I.; Antiochia, R.; Magno, F. An Extended Method for the Practical Evaluation of the Standard Rate Constant from Cyclic Voltammetric Data. *Electroanalysis* 2004, 16, 505-506.
6. Méndez-Vilas, A.; Jódar-Reyes, A. B.; González-Martín, M. L. Ultrasmall Liquid Droplets on Solid Surfaces: Production, Imaging, and Relevance for Current Wetting Research. *Small* 2009, 5, 1366-1390.
7. Rieutord, F.; Salmeron, M. Wetting Properties at the Submicrometer Scale: A Scanning Polarization Force Microscopy Study. *J. Phys. Chem. B* 1998, 102, 3941-3944.
8. Toth, P. S.; Valota, A.; Velicky, M.; Kinloch, I.; Novoselov, K.; Hill, E. W.; Dryfe, R. A. W. Electrochemistry in a Drop: A Study of the Electrochemical Behaviour of Mechanically Exfoliated Graphene on Photoresist Coated Silicon Substrate. *Chem. Sci.* 2014, 5, 582-589.
9. Cottrel, F. G. *Z. Phys. Chem.* 1902, 42, 385.
10. Bard, A. J.; Faulkner, L. R., *Electrochemical Methods. Fundamentals and Applications*. 2nd ed.; John Wiley & Sons, Inc.: New York, 2001.
11. Geim, A. K.; Novoselov, K. S. The Rise of Graphene. *Nat. Mater.* 2007, 6, 183-191.
12. Brownson, D. A. C.; Kampouris, D. K.; Banks, C. E. Graphene Electrochemistry: Fundamental Concepts through to Prominent Applications. *Chem. Soc. Rev.* 2012, 41, 6944-6976.
13. McCreery, R. L. Advanced Carbon Electrode Materials for Molecular Electrochemistry. *Chem. Rev. (Washington, DC, U. S.)* 2008, 108, 2646-2687.
14. Díaz, J.; Paolicelli, G.; Ferrer, S.; Comin, F. Separation of the sp^3 and sp^2 Components in the C1s Photoemission Spectra of Amorphous Carbon Films. *Phys. Rev. B: Condens. Matter Mater. Phys.* 1996, 54, 8064-8069.
15. Jackson, S. T.; Nuzzo, R. G. Determining Hybridization Differences for Amorphous Carbon from the XPS C 1s Envelope. *Appl. Surf. Sci.* 1995, 90, 195-203.
16. Mérel, P.; Tabbal, M.; Chaker, M.; Moisa, S.; Margot, J. Direct Evaluation of the sp3 Content in Diamond-Like-Carbon Films by Xps. *Appl. Surf. Sci.* 1998, 136, 105-110.